8

Machine Learning and Deep Learning Applications in Medical Image Analysis

Pingfan Hu[1], Changjie Cai[2], Yu Feng[3], and Qingsheng Wang[1]

[1] *Artie McFerrin Department of Chemical Engineering, Texas A&M University, College Station, TX, USA*
[2] *Department of Occupational and Environmental Health, Hudson College of Public Health, The University of Oklahoma, Oklahoma City, OK, USA*
[3] *School of Chemical Engineering, Oklahoma State University, Stillwater, OK, USA*

8.1 Introduction

8.1.1 Machine Learning in Medical Imaging

Machine learning algorithms are very effective at using medical imaging to study specific diseases. Numerous machine learning methods have been used to analyze medical images, such as linear discriminant analysis, support vector machines (SVMs), decision trees, and random forests. Pixel/voxel-based machine learning (PML) model emerged in medical image analysis, which uses pixel/voxel values in images directly instead of features calculated from segmented objects as input information (Suzuki 2012). Machine learning algorithms can also combine with the computational aerosol dynamics method for lung disease diagnosis. The exhaled aerosol patterns that were simulated by computational fluid dynamics (CFD) with different asthma conditions were categorized using fractal analysis and SVMs classification as well as random forest (Xi et al. 2015; Xi and Zhao 2019).

8.1.2 Deep Learning in Medical Imaging

Both the 2-dimensional and 3-dimensional structures of an organ being studied are crucial in order to identify what is normal versus abnormal. By maintaining these local spatial relationships, convolutional neural networks (CNNs) are well suited to perform image recognition tasks (Ker et al. 2018). CNNs can also be used for classification, localization, detection, and segmentation (Jiao et al. 2020).
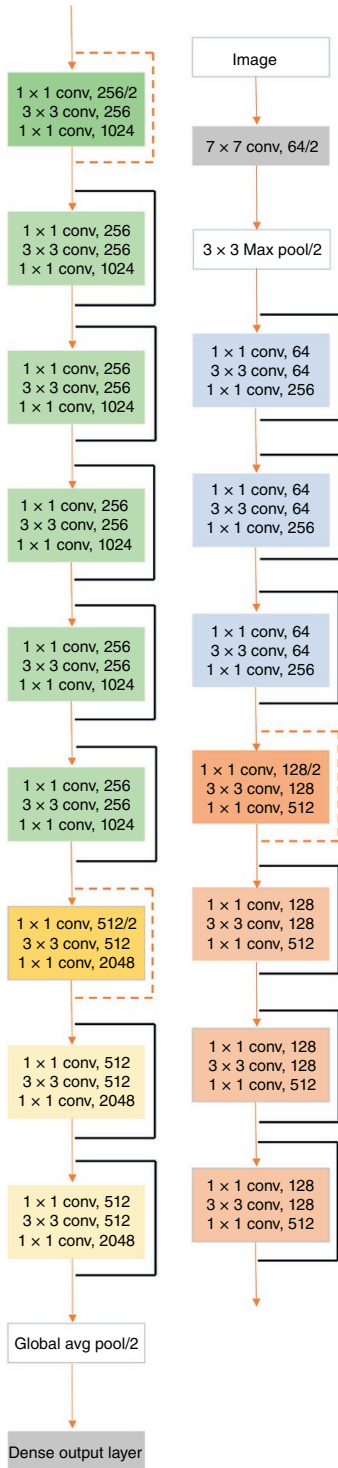
Figure 8.1 Modified ResNet50 architecture.

8.2 CNN-Based Models for Classification

8.2.1 ResNet50

As shown in Figure 8.1, ResNet50 is a 50-layer residual network. The main goal is to build a deeper neural network based on a modified ResNet50 without encountering the vanishing gradient problem (Hochreiter et al. 2001). The error gradients are computed at the end of the network. Backpropagation (Goodfellow et al. 2016) is used to propagate the error gradients backward through the network. Using the chain rule (Goodfellow et al. 2016), terms are multiplied with the error gradients and have to be kept as the networks go backward. However, in the long chain of multiplication, the gradient becomes very small as networks approach the earlier layers in a deep architecture. This small gradient is an issue because network parameters cannot be updated by a large enough amount and the training is very slow. To avoid the vanishing gradient problem, ResNet50 stacks these residual blocks together where an identity function is used to preserve the gradient. It is also called skip connection since the origin input is added to the output of the convolution block directly. The structure of the skip connection is shown in Figure 8.2 (He et al. 2016).

As shown in Figure 8.1, the input image goes through the first layer with 64 filters, with a filter size of 7×7. Next, it goes through the max-pooling layer, which helps reduce the spatial size of the convolved features and helps reduce the over-fitting problem. Then, it goes through 48 convolutional layers with skip connection and finally reaches the fully connected layer that helps learn nonlinear combinations of the high-level features outputted by previous layers. In the modified ResNet50 model employed in this study, parameters of the pretrained convolutional layers on the ImageNet dataset (Deng et al. 2009) were used. The final pooling and fully connected layer in the original ResNet50 model were replaced by global average pooling and a dense output layer, in order to connect the dimensions of the previous layers with the new layers for classification of our own dataset. Regularization methods (e.g. batch normalization and dropout) and optimizers were used to avoid over-fitting and reduce computational time (He et al. 2016).
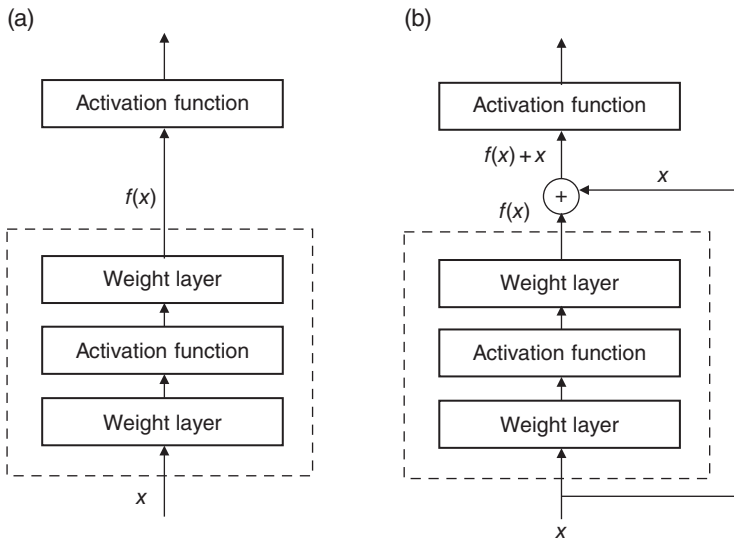
(a)

(b)

Figure 8.2 The residual learning building blocks: (a) regular block and (b) residual block.

8.2.2 YOLOv4 (Darknet53)

One popular state-of-the-art CNN-based model for detecting objects in an image is "You Only Look Once" or YOLO (Redmon et al. 2016). YOLO version 3 (YOLOv3) expands on its previous version, YOLOv2, by utilizing a Darknet53 (53 convolutional layers) as its backbone in contrast to YOLOv2, which utilized Darknet19 (19 convolutional layers) (Redmon and Farhadi 2017). Although the precision has been greatly improved in YOLOv3 compared with YOLOv2 due to the increased number of convolutional layers, the resultantly increased computational complexity also makes YOLOv3 more computationally expensive. To optimize the balance between precision and computational efficiency, YOLOv4 has been developed to improve both the precision and speed of YOLOv3. YOLOv4 is considered as one of the most accurate real-time neural network detectors to date (Bochkovskiy et al. 2004). YOLOv4 has been successfully applied in various industries, including autonomous driving, agriculture, electronics, public health, etc. (Li et al. 2020; Cai et al. 2021; Kajabad et al. 2021; Sozzi et al. 2021). In this study, YOLOv4 was employed and tested for classifying the lung obstruction locations, including left lung, right lung, and both lungs.

YOLOv4 consists of three main blocks, including the "backbone," "neck," and "head" (Bochkovskiy et al. 2004). The "backbone" implements feature extraction. The model implements the Cross Stage Partial Network (CSPNet) backbone method to extract features (Wang et al. 2020), containing 53 convolutional layers for accurate image classification, also known as CSPDarknet53. The "neck" is a layer between the "backbone" and "head" that implements feature aggregation. Specifically, YOLOv4 uses the Path Aggregation Network (PANet) for feature aggregation (Liu et al. 2018) and Spatial Pyramid Pooling (SPP) method to set apart the important features obtained from the "backbone" (Liu et al. 2018). The "head" used in YOLOv4 is the same as the one in YOLOv3, which uses dense prediction

for anchor-based detection that helps divide the image into multiple cells and inspect each cell to find the probability of having an object using the post-processing techniques (Redmon et al. 2016).

8.2.3 Grad-CAM

In practice, deep learning models are treated as "black box" methods. To enhance the fundamental understanding of where the CNN-based models are "looking" in the input image, a simple modification of the global average pooling layer combined with Grad-CAM (Rajasegarar et al. 2007) allows the classification-trained CNN to both classify the image and localize class-specific image regions. The gradient of the chosen convolutional layer is converted to weight. Then the 1D vector that stored the number of filters is reshaped to the image shape. After the layer output and weight are computed and normalized, the heat map showing the highly correlated regions of input for predictions is created. By generating such visual explanations, Grad-CAM makes the CNN-based model more transparent and insightful.

8.3 Case Study

8.3.1 Background

According to the National Vital Statistics Report (Hamilton et al. 2013), chronic obstructive pulmonary disease (COPD) is the third leading cause of death in America. COPD causes severe breathing difficulty due to airway stiffening, loss of airway deformation capability, and airway blockage induced by inflammation especially in small airways, which are regarded as the silent zone in the respiratory system (Yi et al. 2021; Rajendran and Banerjee 2020; Pramanik et al. 2021). Inhalation of therapeutic nano-/microparticles is the standard COPD treatment, but delivering a sufficiently high dose of therapeutic nano-/microparticles to obstruction sites in small airways has remained the long-standing barrier preventing the desired therapeutic outcomes.

To overcome such a barrier, it is important to detect the obstruction locations in small airways of COPD patients at an early stage and optimize the inhalation therapy to achieve targeted drug delivery to designated obstruction sites, instead of healthy airway tissues, for better therapeutic outcomes and reduced side effects. However, there is strong evidence to suggest that most patients are not aware of their small airway obstruction conditions at the early stage, due in part to the invasive nature of conventional diagnostic methods (Jindal 2012; Burgel et al. 2013; Deepak et al. 2017). Specifically, traditional methods to diagnose pulmonary diseases involve costly and invasive procedures such as X-ray screening and bronchoscope. Thus, it is imperative and beneficial to detect the obstruction locations in the peripheral lung precisely with noninvasive diagnostic methods.

This case study proposes and tests the feasibility of a new diagnostic methodology using both CFD and CNN. The new methodology is able to identify the obstruction location in the left lung, right lung, or both lungs using hyperpolarized magnetic resonance imaging (MRI)

(Salerno et al. 2001; Walkup and Woods 2014; Roos et al. 2015; Walkup et al. 2016). The method was driven by a central hypothesis enlightened by existing preliminary studies (Sul et al. 2018). The small airway obstruction will lead to detectable velocity distribution pattern shift of the expiratory airflow in the trachea. Specifically, based on the training and test data generated using the CFD simulation results of expiratory airflows in a subject-specific human tracheobronchial tree (trachea to G6), two CNN-based classification models were developed using open-source codes, e.g. ResNet50 and YOLOv4 (Darknet53) (Bochkovskiy et al. 2004). The modified ResNet50 model is a 50-layer residual network, and it was the winner of the ImageNet Large Scale Visual Recognition Challenge (ILSVRC) in 2015. The main goal of the residual network is to build a deeper neural network without the problem of vanishing gradients. To further analyze which regions suggest the obstruction locations, Gradient-weighted Class Activation Mapping (Grad-CAM) was applied to produce a coarse localization map highlighting the important regions (Daibo 2017). The results have also been validated by Darknet53, which acts as a backbone for the YOLOv4 object detection approach. (Li et al. 2020; Cai et al. 2021; Kajabad et al. 2021; Sozzi et al. 2021).

Two CNN-based models, e.g. modified ResNet50 and YOLOv4, are trained by CFD expiratory velocity contours in a subject-specific 3D tracheobronchial (TB) tree with 990 obstruction conditions at small airway terminals to automatically classify COPD airway obstruction locations. Grad-CAM and hue-value-saturation (HSV) thresholding techniques were employed to classify COPD obstruction locations and velocity contour pattern shifts in the lung and highlight the highly correlated regions in the contours for locating the obstruction sites.

8.3.2 Study Design

Based on the central hypothesis, the workflow of the training and test of the two CNN classification models are shown in Figure 8.3a and b. A subject-specific TB tree from the trachea to G6 was employed for the expiratory flow simulations using CFD. An experimentally validated CFD model (Feng et al. 2018) was employed to predict expiratory intrathoracic flow velocity distributions through the TB tree with 1 normal airway and 990 airway obstruction conditions. Using the airflow velocity distribution data labeled by the obstruction locations, two CNN-based classification models were trained and tested.

8.3.3 Training and Testing Database Preparation

As shown in Figure 8.3a and b, the preparation of the training and test database used the CFD simulation results for the expiratory flow field predictions with different obstruction conditions in the subject-specific TB tree. Specifically, only 1 or 2 of the 44 small airway openings were blocked for each simulation case in order to mimic the minimum changes in obstruction conditions in the human lung compared with the obstructions of multiple openings in left, right, or both lungs. The structure of the labeled training and test images is shown in Figure 8.4.
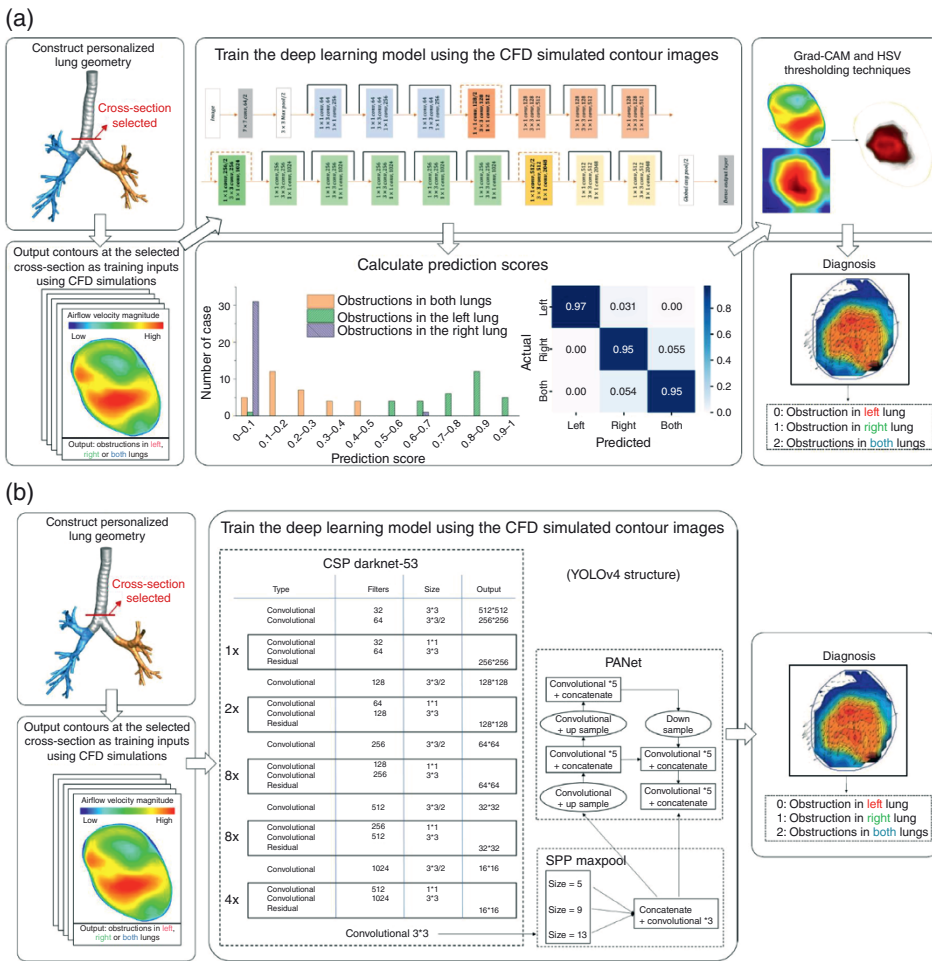
Figure 8.3 Workflows of CNN development to diagnose obstructed locations in the human lung based on expiratory flow patterns: (a) ResNet50 and (b) YOLOv4 (Darknet53).

The velocity contours used for training and testing the two CNN-based models were acquired at a selected cross-section ($x = 0.1$ m) for all CFD simulation cases. The cross-section was selected based on two rationales: (i) the available locations in the chest where the airflow velocity distributions can be measured by hyperpolarized MRI and (ii) the location that is closer to the obstruction sites at 44 small airway terminals. Specifically, the closer the selected cross-section and the obstruction sites are, the more negligible the dissipation effect will be, and the more identifiable shifts of the airflow velocity distributions can be maintained due to the variation in deeper-lung expiratory flow conditions induced by the obstruction. An example of the expiratory velocity contour at $x = 0.1$ m can be found in Figure 8.3a and b. The images were partitioned into training and testing sets for each obstruction class, with an approximately 80 to 20% split and fivefold cross-validation.
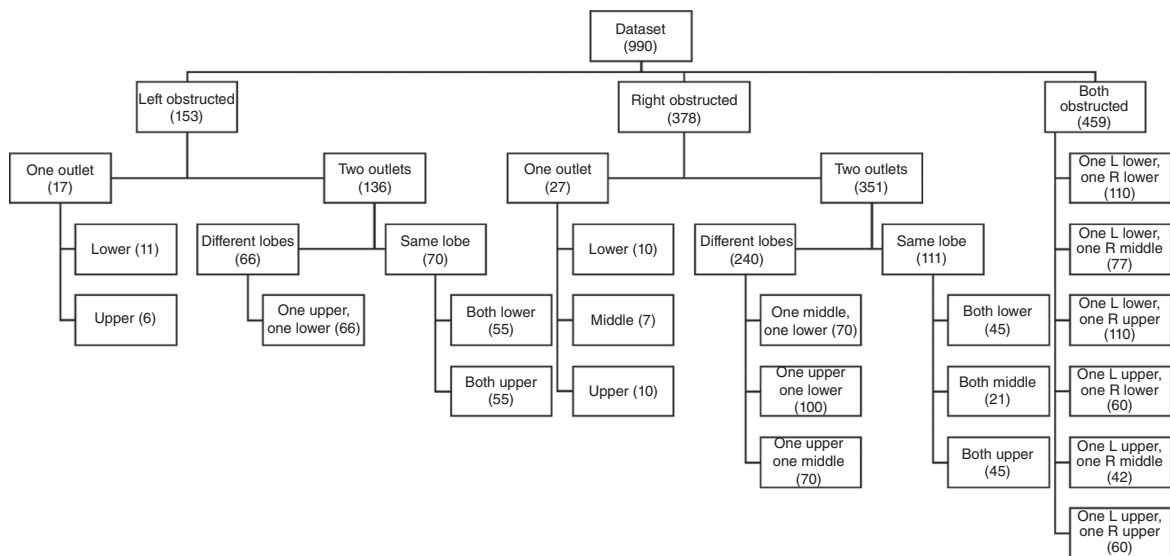
Figure 8.4 Data structure of the training and test images prepared using CFD.

8.3.4 Results

8.3.4.1 Classification Performance of the Modified ResNet50 Model

The performance of the modified ResNet50 model is visualized by both the histogram of prediction scores (see Figure 8.5) and the confusion matrix heat map (see Figure 8.6). The prediction scores of all test cases for left lung, right lung, and both lung obstructions are shown in Figure 8.5a–c, respectively. The high score in each category indicates that the model has a high certainty, and the case will be classified based on the highest prediction score's class. As shown in Figure 8.5a–c, most of the test cases have the highest prediction scores in the class with the same obstruction locations, which indicates the reliability of the prediction score system. Furthermore, as shown in Figure 8.6 and Table 8.1, the testing dataset performance quantified by the average precision (AP) at a threshold of 0.5 is:

- Left lung obstructed: AP = 89.27%
- Right lung obstructed: AP = 93.89%
- Both lungs obstructed: AP = 98.43%

The total accuracy converges to 95.1% after 20 epochs. Based on the testing result, the modified ResNet50 model is a reliable classifier to identify whether the obstruction is in the left lung, right lung, or both lungs with high sensitivity. The no obstruction case (e.g. normal airways) was studied, and the scores for both obstructions, left obstructions, and right obstructions are 0.3785, 0.3337, and 0.2878, respectively. Thus, the model is able to distinguish between obstruction cases and the healthy no-obstruction case.

8.3.4.2 Classification Performance of the YOLOv4 Model

To validate the modified ResNet50 model for classification and compare the sensitivity of AP to different CNN-based models, the YOLOv4 model was trained by conducting two tests (see Table 8.1). In the first test (e.g. Test 1), to have a similar number of images for each class during training, we randomly selected 153, 153, and 153 images for left, right, and both lung obstructions, respectively. The values of precision (P), recall (R), and $F1$ *score* are listed in Table 8.1. Specifically, precision (P) represents the ability of the classifier to identify relevant data points that were classified as true and that were actually true. Recall (R) is described as the ability of the classifier to find all relevant data points. Maximizing P often comes at the expense of R and vice versa. The $F1$ *score* is considered as a parameter that can reflect both P and R more objectively. Determining the $F1$ *score* is useful in this assessment to ensure optimal precision (P) and recall scores (R) can be achieved. As shown in Table 8.1, the precision, recall, and $F1$ score are 0.93, 0.94, and 0.93 at a threshold of 0.5 for Test 1, respectively. By checking the AP for each class, the recognition of right lung ($AP = 96.78\%$) and both lung ($AP = 93.85\%$) obstructions were not as good as recognition of the left lung obstruction ($AP = 100\%$). Therefore, the second test (e.g. Test 2) doubled the "right lung obstructed" images (from 153 to 378) and tripled the "both lung obstructed" images (from 153 to 459). APs slightly increased for the two classes (e.g. from 96.78 to 97.74% for right lung obstructions and from 93.85 to 96.29% for both lung obstructions). Thus, the overall YOLOv4 model trained in Test 2 is slightly better than Test 1, with P increased from
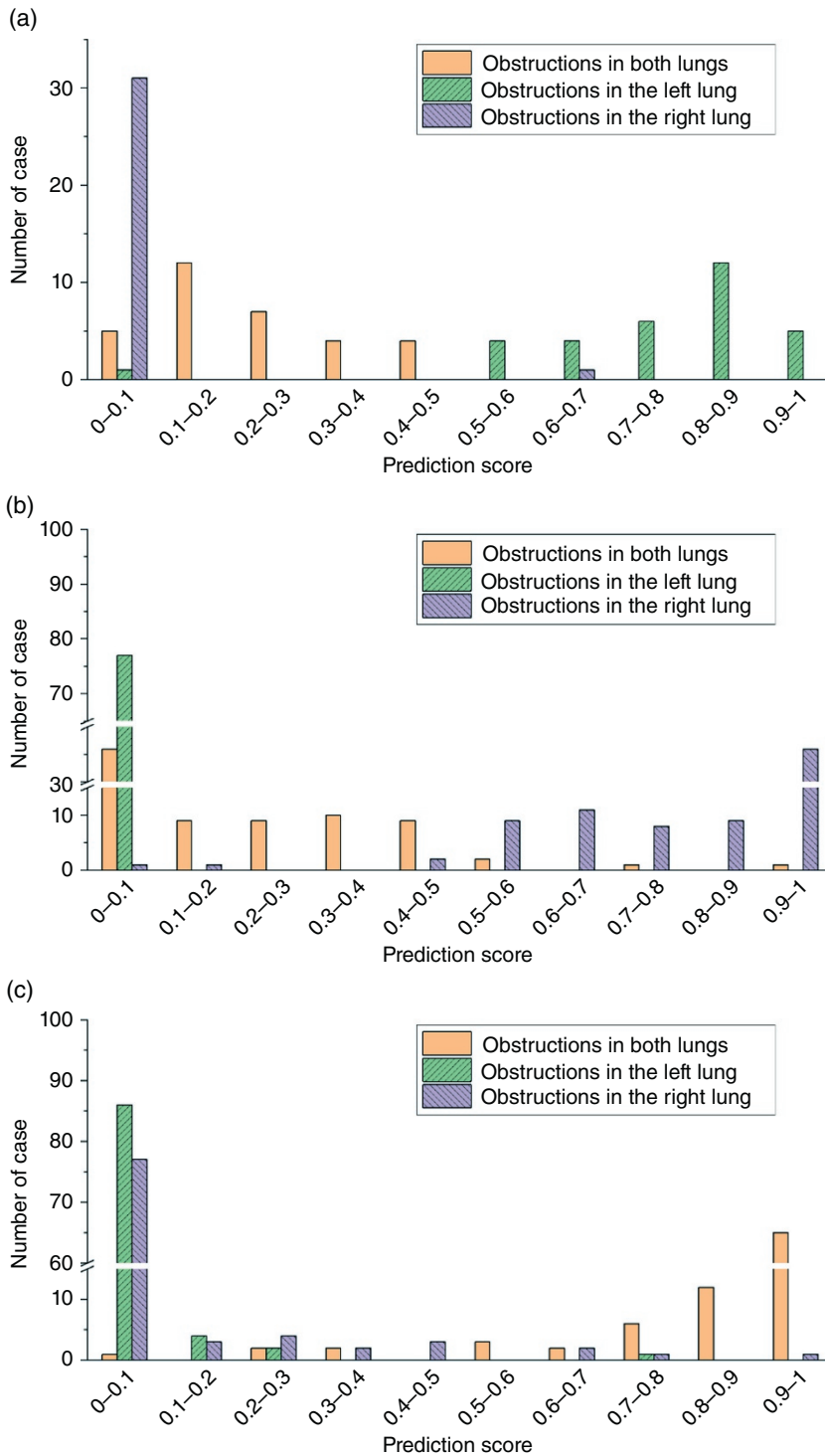
Figure 8.5 Prediction scores for (a) left lung obstructions, (b) right lung obstructions, and (c) both lungs obstructions.
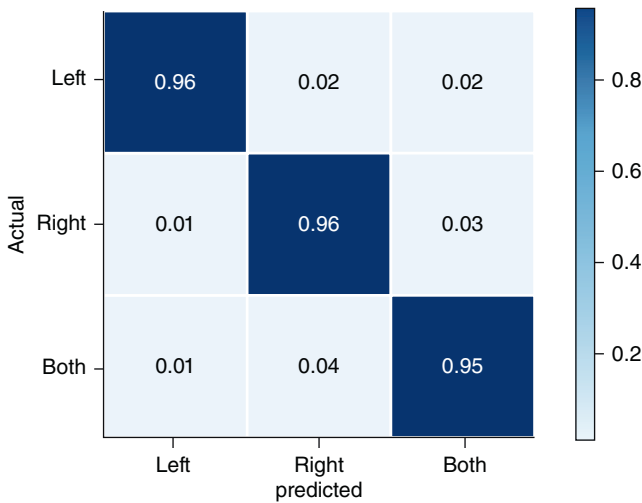
Figure 8.6 Confusion matrix heat map for prediction.

Table 8.1 Evaluation metrics of modified Resnet50 and YOLOv4 models.

Evaluation metrics	ResNet50 test[a](%)	YOLOv4 test 01[b](%)	YOLOv4 test 02[c](%)
Macro precision $P = TP/(TP + FP)$	93.86	93.00	96.00
Macro recall $R = TP/(TP + FN)$	95.27	94.00	97.00
F1 score $F1 = 2PR/(P + R)$	94.56	93.00	96.00
Average precision (AP) (Left lung obstructed)	89.27	100%	100%
Average precision (AP) (Right lung obstructed)	93.89	96.78	97.74
Average precision (AP) (Both lungs obstructed)	98.42	93.85	96.29

TP, true positive; FP, false positive; FN, false negative.
[a] ResNet50 Test : 153 images for left, 378 images for right, and 459 images for both lung obstructions.
[b] YOLO Test 01 : 153 images for left, 153 images for right, and 153 images for both lung obstructions.
[c] YOLO Test 02 : 153 images for left, 378 images for right, and 459 images for both lung obstructions.

0.93 to 0.96, *R* increased from 0.94 to 0.97, and *F*1 score increased from 0.93 to 0.96. The comparison of evaluation results between the modified ResNet50 and YOLOv4 models summarized in Table 8.1 shows that both models can be used as classifiers for the obstruction location identifications. The modified ResNet50 model was coded and compiled in Keras 2.4.3. It was run on Windows Operating System with GPU (GeForce RTX 2080 with 16 GB-VRAM). The training computation is approximately 12 seconds per epoch with 19 minutes and 10 seconds in total. The YOLOv4-based CNN model was compiled in Microsoft Visual Studio 2019 (Microsoft Corporation, Albuquerque, NM, USA) and run

on Windows Operating System with GPU (GeForce GTX 1660 Ti with 16 GB-VRAM), CUDNN_HALF, and OpenCV for accelerating the training. For test02, the training computation is approximately 10 seconds per iteration with batch-size of 64, subdivisions (or mini batch-size) of 64, and 6000 iterations in total; therefore, the training computation performance is approximately 130 seconds per epoch with 18 hours and 17 minutes in total. Considering the computational costs, the modified ResNet50 is more efficient than YOLOv4.

8.3.4.3 Post-Processing Via Grad-CAM Model and HSV

As shown in Figure 8.7, the Grad-CAM model is combined with the modified ResNet50 model to output the heat map visualization of the important region. The HSV thresholding technique is applied to the heat map plot of the Grad-CAM model. The HSV color space is a cylindrical coordinate representation of points in an RGB color model. It represents the human perception using Hue (the dominant color as perceived by an observer), Saturation (the amount of white light mixed with a Hue), and Value (the chromatic notion of intensity). The highlighted regions were detected by filtering out the color that suggests a low correlation with the obstructions. As shown in Figure 8.8, the highlighted regions for cases within the same obstruction class (e.g. left lung, right lung, or both lungs) were blended with the same weight to assist in finding the most important regions to identify different obstructions. The brightness of the color shows the importance of the region for classification. It can be observed that the area of the bright red region for both lung obstructions is larger than those for left or right lung obstruction cases. It indicates that the determination of both lung obstructions requires more information.
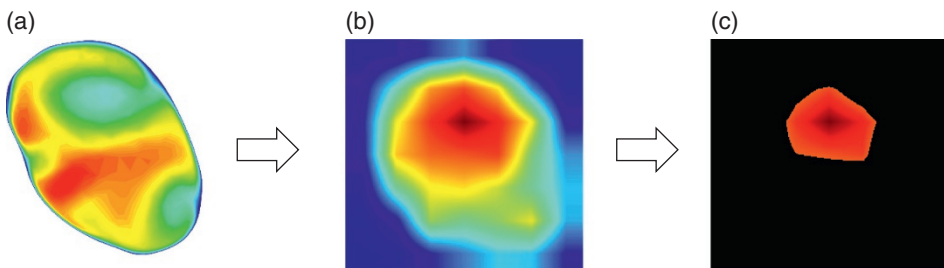
(a)　　　　　　　　　　(b)　　　　　　　　　　(c)

Figure 8.7　HSV thresholding technique procedure: (a) CFD model output, (b) Grad-CAM model output, (c) high correlation region for obstruction.
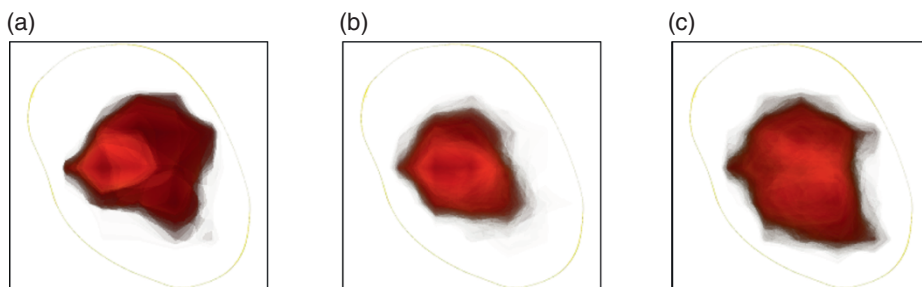
(a)　　　　　　　　　　(b)　　　　　　　　　　(c)

Figure 8.8　Blended highlight regions of construction for (a) left lung, (b) right lung, and (c) both lungs.

8.3.5 Conclusion

The prototype of a novel, effective, and noninvasive tool for early diagnosis of deeper airway obstructions has been developed using CFD and two CNN-based models. The important regions have been determined by Grad-CAM and HSV thresholding techniques and confirmed by the Pearson correlation coefficient calculations between CFD velocity contours. The reason for the falsely classified cases was analyzed based on the comparisons of fundamental airflow dynamics in the intrathoracic region. Key conclusions are summarized as follows:

1) The two CNN-based models (e.g. modified ResNet50 and YOLOv4) can detect small airway obstruction locations based on measurable expiratory airflow patterns in the intrathoracic region well with all evaluation scores higher than 93%, including precision, recall, *F1* score, and average precisions. YOLOv4 is slightly better in classification performance than the modified ResNet50 but requires a higher computational cost. Furthermore, the results of the two CNN-based models validate each other very well. The bagging or boosting ensemble method can be applied to achieve better overall prediction accuracy.
2) The comparisons of expiratory velocity contours show minor flow field pattern shifts with the variations of obstruction sites and demonstrate the necessity of employing CNN algorithms for the effective diagnosis of obstructions. In addition, the Pearson correlation coefficients show much lower similarities of the velocity contours in the highly correlated region identified by CNN-based models than the velocity contours of the whole cross-section, which explains why the Grad-CAM and HSV techniques rely more on the high-correlated regions to identify the obstruction locations.

This prototype of the diagnostic algorithms paves the way for the development of noninvasive and effective diagnostic tools with classification algorithms to effectively diagnose COPD at an early stage and provide high-resolution information for precise treatment (e.g. targeted drug delivery to the identified obstruction sites) with better therapeutic outcomes. No CFD knowledge is needed for users (e.g. physicians) to use the classification algorithm, which increases the transformative impact of the CNN-based models for clinical practice.

8.4 Limitations and Future Work

The present study developed a prototype of the diagnostic algorithm to identify lung obstruction locations via the expiratory airflow distributions in the trachea, integrating CFD and CNN. Limitations of the study are listed as follows:

1) Only one subject-specific TB tree configuration was employed in the CFD simulation for the preparation of training and test images, which did not consider the intersubject variability effect and the influence of airway deformation kinematics.
2) Obstructions were assumed to only appear in either the left lung, the right lung, or both lungs in the training and test images, which could be more specific to different lobes.

3) The airway was assumed to be rigid, which neglected the effect of airway expansion and contraction in the real-world breathing process.
4) The input images were produced by the CFD instead of real-world MRI images.

To address the limitations of the present study and further develop a diagnosis algorithm that can be ready for clinical practice, future work includes:

1) More subject-specific airway configurations with airway deformation kinematics will be obtained and employed in the CFD simulations to prepare the training and test images with the effect of intersubject variabilities, which will enhance the generalized predictability of the CNN algorithm.
2) Lobe-specific obstruction diagnosis will be achieved by improving the training process of the two CNN-based models.
3) Noises and missing parts could be added to mimic the real-world MRI images first and then replaced by hyperpolarized MRI images to further improve the accuracy and realism of the CNN algorithms.

The long-term goal is to provide physicians with a computationally efficient diagnosis algorithm, which can identify the obstruction locations in human lungs based on the pulmonary airflow velocity distributions that are measurable using hyperpolarized MRI (Salerno et al. 2001; Walkup and Woods 2014; Roos et al. 2015; Walkup et al. 2016).

References

Bochkovskiy, A., Wang, C.-Y., and Liao, H.-Y.M. (2004). Yolov4: optimal speed and accuracy of object detection. *arXiv preprint arXiv:2004.10934, 2020*.

Burgel, P.-R., Bergeron, A., De Blic, J. et al. (2013). Small airways diseases, excluding asthma and COPD: an overview. *European Respiratory Review* 22 (128): 131–147.

Cai, C., Nishimura, T., Hwang, J. et al. (2021). Asbestos detection with fluorescence microscopy images and deep learning. *Sensors* 21 (13): 4582.

Daibo, M. (2017). Toroidal vector-potential transformer. *2017 Eleventh International Conference on Sensing Technology (ICST)*, Sydney, Australia (4–6 December 2017). IEEE.

Deepak, D., Prasad, A., Atwal, S.S., and Agarwal, K. (2017). Recognition of small airways obstruction in asthma and COPD – the road less travelled. *Journal of Clinical and Diagnostic Research: JCDR*. 11 (3): TE01–TE05.

Deng, J., Dong, W., Socher, R., et al. (2009). Imagenet: a large-scale hierarchical image database. *2009 IEEE Conference on Computer Vision and Pattern Recognition*, Miami, FL (20–25 June 2009). IEEE.

Feng, Y., Zhao, J., Kleinstreuer, C. et al. (2018). An in silico inter-subject variability study of extra-thoracic morphology effects on inhaled particle transport and deposition. *Journal of Aerosol Science*. 123: 185–207.

Goodfellow, I., Bengio, Y., and Courville, A. (2016). *Deep Learning*. MIT Press.

Hamilton, B.E., Hoyert, D.L., Martin, J.A. et al. (2013). Annual summary of vital statistics: 2010–2011. *Pediatrics* 131 (3): 548–558.

He, K., Zhang, X., Ren, S., and Sun, J. (2016). Deep residual learning for image recognition. Proceedings of the IEEE Conference on Computer Vision and Pattern Recognition, Las Vegas, NV, USA (27–30 June 2016).

Hochreiter, S., Bengio, Y., Frasconi, P., and Schmidhuber, J. (2001). Gradient flow in recurrent nets: the difficulty of learning long-term dependencies. In: *A field guide to dynamical recurrent neural networks*. IEEE Press.

Jiao, Z., Hu, P., Xu, H., and Wang, Q. (2020). Machine learning and deep learning in chemical health and safety: a systematic review of techniques and applications. *ACS Chemical Health & Safety* 27 (6): 316–334.

Jindal, S.K. (2012). COPD: the unrecognized epidemic in India. *The Journal of the Association of Physicians of India* 60 (Suppl): 14–16.

Kajabad, E.N., Begen, P., Nizomutdinov, B., and Ivanov, S. (2021). YOLOv4 for urban object detection: case of electronic inventory in St. Petersburg. *2021 28th Conference of Open Innovations Association (FRUCT),* Moscow, Russia (27–29 January 2021). IEEE.

Ker, J., Wang, L., Rao, J., and Lim, T. (2018). Deep learning applications in medical image analysis. *IEEE Access.* 6: 9375–9389.

Li, Y., Wang, H., Dang, L. et al. (2020). A deep learning-based hybrid framework for object detection and recognition in autonomous driving. *IEEE Access.* 8: 194228–194239.

Liu, S., Qi, L., Qin, H., Shi, J., and Jia, J. (2018). Path aggregation network for instance segmentation. Proceedings of the IEEE Conference on Computer Vision and Pattern Recognition, Salt Lake City, UT, USA (18–23 June 2018).

Pramanik, S., Mohanto, S., Manne, R. et al. (2021). Nanoparticle-based drug delivery system: the magic bullet for the treatment of chronic pulmonary diseases. *Molecular Pharmaceutics* 18 (10): 3671–3718.

Rajasegarar, S., Leckie, C., Palaniswami, M., and Bezdek, J. C. (2007). Quarter sphere based distributed anomaly detection in wireless sensor networks. *2007 IEEE International Conference on Communications,* Glasgow, Scotland (24–28 June 2007). IEEE.

Rajendran, R.R. and Banerjee, A. (2020). Effect of non-Newtonian dynamics on the clearance of mucus from bifurcating lung airway models. *Journal of Biomechanical Engineering* 143 (2): 021011.

Redmon, J. and A. Farhadi. (2017). YOLO9000: better, faster, stronger. Proceedings of the IEEE Conference on Computer Vision and Pattern Recognition, Honolulu, HI, USA (21–26 July 2017).

Redmon, J., Divvala, S., Girshick, R., and Farhadi, A. (2016). You only look once: unified, real-time object detection. Proceedings of the IEEE Conference on Computer Vision and Pattern Recognition, Las Vegas, NV, USA (27–30 June 2017).

Roos, J.E., McAdams, H.P., Kaushik, S.S., and Driehuys, B. (2015). Hyperpolarized gas MR imaging: technique and applications. *Magnetic Resonance Imaging Clinics of North America* 23 (2): 217–229.

Salerno, M., Altes, T.A., Brookeman, J.R. et al. (2001). Dynamic spiral MRI of pulmonary gas flow using hyperpolarized 3He: preliminary studies in healthy and diseased lungs. *Magnetic Resonance in Medicine: An Official Journal of the International Society for Magnetic Resonance in Medicine.* 46 (4): 667–677.

Sozzi, M., Cantalamessa, S., Cogato, A. et al. (2021). Grape yield spatial variability assessment using YOLOv4 object detection algorithm. In: *Precision Agriculture'21*, 193–198. Wageningen Academic Publishers.

Sul, B., Oppito, Z., Jayasekera, S. et al. (2018). Assessing airflow sensitivity to healthy and diseased lung conditions in a computational fluid dynamics model validated in vitro. *Journal of Biomechanical Engineering* 140 (5).

Suzuki, K. (2012). Pixel-based machine learning in medical imaging. *International Journal of Biomedical Imaging* 2012: 1.

Walkup, L.L. and Woods, J.C. (2014). Translational applications of hyperpolarized 3He and 129Xe. *NMR in Biomedicine* 27 (12): 1429–1438.

Walkup, L.L., Thomen, R.P., Akinyi, T.G. et al. (2016). Feasibility, tolerability and safety of pediatric hyperpolarized 129 Xe magnetic resonance imaging in healthy volunteers and children with cystic fibrosis. *Pediatric Radiology* 46 (12): 1651–1662.

Wang, C.-Y., Liao, H. Y. M., Wu, Y. H., et al. (2020). CSPNet: a new backbone that can enhance learning capability of CNN. Proceedings of the IEEE/CVF Conference on Computer Vision and Pattern Recognition Workshops, Virtual (13–19 June 2020), 671.

Xi, J. and Zhao, W. (2019). Correlating exhaled aerosol images to small airway obstructive diseases: a study with dynamic mode decomposition and machine learning. *PLoS One* 14 (1): e0211413.

Xi, J. et al. (2015). Detecting lung diseases from exhaled aerosols: non-invasive lung diagnosis using fractal analysis and SVM classification. *PLoS One* 10 (9): e0139511.

Yi, H., Wang, Q., and Feng, Y. (2021). Computational analysis of obstructive disease and cough intensity effects on the mucus transport and clearance in an idealized upper airway model using the volume of fluid method. *Physics of Fluids* 33 (2): 021903.